MIT Open Access Articles

Tuning Electrical, Optical, and Thermal Properties through Cation Disorder in Cu2ZnSnS4

Tuning electrical, optical, and thermal properties through cation disorder in Cu_2ZnSnS_4

Kevin Ye[1], Sin Cheng Siah[2], Peter T. Erslev[3], Austin Akey[4], Charles Settens[5], Md Shafkat Bin Hoque[6], Jeffrey Braun[6], Patrick Hopkins[6,7,8], Glenn Teeter[3], Tonio Buonassisi[2], R. Jaramillo[1]

[1]Department of Materials Science and Engineering, Massachusetts Institute of Technology, 77 Massachusetts Ave., Cambridge, MA 02139, USA

[2]Department of Mechanical Engineering, Massachusetts Institute of Technology, 77 Massachusetts Ave., Cambridge, MA 02139, USA

[3]National Center for Photovoltaics, National Renewable Energy Laboratory, 15013 Denver West Parkway, Golden, CO 80401, USA

[4]Center for Nanoscale Systems, Harvard University, Cambridge, MA 02138 USA

[5]Materials Research Laboratory, Massachusetts Institute of Technology, 77 Massachusetts Ave., Cambridge, MA 02139, USA

[6]Department of Mechanical and Aerospace Engineering, University of Virginia, Charlottesville, VA 22904 USA

[7]Department of Materials Science and Engineering, University of Virginia, Charlottesville, VA 22904 USA

[8]Department of Physics, University of Virginia, Charlottesville, VA 22904 USA

Abstract

Chemical disorder in semiconductors is important to characterize reliably because it affects materials performance, for instance by introducing potential fluctuations and recombination sites. It also represents a means to control material properties, to far-exceed the limits of equilibrium thermodynamics. We present a study of highly-disordered Cu-Zn-Sn-S (d-CZTS) films along the Cu_2SnS_3 – Cu_2ZnSnS_4 – ZnS binary line, deposited by physical vapor deposition. Deposition at low temperature kinetically stabilizes compositions that are well outside of the narrow, equilibrium solid solution of kesterite (Cu_2ZnSnS_4). Here we study d-CZTS and its thermal treatment using complementary characterization techniques: X-ray absorption spectroscopy (XAS), X-ray diffraction (XRD), and transmission electron microscopy (TEM). We find that cations in d-CZTS are highly-disordered while the sulfur anions remain in a well-defined, cubic close-packed lattice. On the atomic scale, composition fluctuations are accommodated preferentially by stacking faults. Kinetically-stabilized cation disorder can produce non-equilibrium semiconductor alloys with a wide range of band gap, electronic conductivity, and thermal conductivity. d-CZTS therefore represents a processing route to optimizing materials for optoelectronic device elements such as light absorbers, window layers, and thermal barriers.

1. Introduction: Cation disorder in CZTS

Kesterite Cu_2ZnSnS_4 (CZTS) has long been of interest as an absorber for thin film photovoltaics (PV), but the record conversion efficiency of CZTS PV devices remains below 13%.[1] CZTS is a good light absorber with a direct band gap of $E_g = 1.5$ eV, which can be reduced by selenium alloying.[2] The tetragonal unit cell and tetrahedral coordination are derived from the diamond cubic structure of Si by four stages of aliovalent pair substitution obeying the octet rule: from Si to a III-V material (*e.g.* GaAs), to a II-VI material (*e.g.* ZnS), to a I-III-VI$_2$ material (*e.g.* chalcopyrite $CuInS_2$), to I$_2$-II-VI-VI$_2$ (*i.e.* kesterite Cu_2ZnSnS_4). It is thought that the PV performance deficit is due in large to cation disorder, such as Zn_{Cu} and Cu_{Zn} antisites that are common due to the chemical similarity of Zn^{2+} and Cu^{1+} cations.[3] Cation disorder can cause band gap fluctuations, electrostatic potential fluctuations, and defect-assisted recombination levels, all of which limit the photovoltage.[4–6]

Due to its impact on PV performance, and also due to the experimental challenges involved, cation disorder in CZTS has been the focus of many studies.[3–11] Above $T_{C2} = 876$ °C, the equilibrium structure is cubic sphalerite (ZnS-like).[3] In this crystal, there is only one cation site and the cations are randomly distributed. Between T_{C2} and $T_{C1} = 260$ °C, the equilibrium structure is tetragonal with space group $I\bar{4}2m$ (very similar to the structure of $CuInS_2$ (CIS) with space group $I\bar{4}2d$).[7] In this crystal, Sn are ordered, while Zn and Cu are randomly distributed. Below T_{C1} the equilibrium structure is kesterite (space group $I\bar{4}$), with distinct sites for Sn, Zn and Cu. At equilibrium, therefore, with increasing temperature CZTS undergoes two order-disorder transitions with increasing cation disorder, while the anion sites have a fixed, cubic close-packed structure.

Cation disorder in real samples often far exceeds that expected at equilibrium. Samples cooled from above T_{C1} to room-temperature retain a lot of Cu-Zn disorder that depends on the cooling rate.[3,5] Films and particles made at low temperature have high levels of cation disorder and even off-stoichiometry that can far exceed the narrow window of equilibrium solid solubility.[8–10] For instance, we and others have shown that ZnS-rich films with overall composition along the Cu_2SnS_3 – CZTS – ZnS binary line, but well outside the CZTS equilibrium solid solution (*c.f.* **Figure 1**), appear in many ways to be single-phase systems, kinetically trapped away from equilibrium.[12–15] Cu_2SnS_3-rich ceramics have been observed to accommodate stoichiometry variations in a superstructure with nanometer-size domains with more and less cation order.[11] Common characterization techniques can belie the existence of point defect clusters or nanometer-scale phase inhomogeneities that may be present.[4,8–10,16]

Cation disorder represents a means to control material properties through synthesis. For instance, through kinetic stabilization, we can make solid solutions that are thermodynamically metastable or even unstable, and these solutions offer a range of physical properties that is greatly-expanded relative to equilibrium thermodynamics. In this work we address optical, electrical, and thermal properties of highly-disordered CZTS (d-CZTS). Previously, materials processing for cation disorder has been studied for battery cathode materials and as a way to reduce thermal conductivity of thermoelectric materials.[17,18]

Disorder in CZTS is hard to experimentally characterize due to the chemical similarity of Zn^{2+} and Cu^{1+} cations, and because competing phases including as ZnS and Cu_2SnS_3 are structurally-coherent with CZTS. Probes of long-range order include X-ray and neutron diffraction. Conventional X-ray diffraction (XRD) cannot distinguish Zn^{2+} and Cu^{1+} because they have the same electron count. Neutron diffraction and resonant XRD are more reliable for crystallographic refinement of CZTS, and can quantify cation antisites.[3,10,15] Probes of short-range order include X-ray absorption spectroscopy (XAS) and transmission electron microscopy (TEM). XAS can measure local crystal structure and electronic structure: extended X-ray absorption fine structure (EXAFS) can quantify deviations from the ideal kesterite structure of the local coordination environments of particular elements, and X-ray absorption near-edge structure (XANES) can quantify secondary phases by the fingerprint of their molecular orbital electronic structure.[10,12,13,19] Cation disorder can be seen directly by high-resolution TEM.[11,16] Structural disorder can also be studied indirectly by its effects on electronic disorder, which is evident in measurements such as photoluminescence spectroscopy and quantum efficiency.[5,6]

In this work we emphasize the techniques XRD, XAS, and TEM, and the complementary evidence they provide about the nature of cation disorder in d-CZTS thin films. High levels of cation disorder can produce experimental signatures of an amorphous material despite the presence of an ordered, close-packed anion lattice; multiple, complementary characterization techniques are needed to determine phase and microstructure. This insight may be broadly applicable to experimental studies on disordered alloys and amorphous materials, such as phase-change chalcogenides. d-CZTS films grown at room temperature can accommodate a wide range of non-equilibrium compositions, which partially resolve by phase separation after thermal treatment. This highly-tunable metastable phase may be useful for designing light absorbers, window layers, electronic contacts, or thermal control layers. We present measurements showing that electrical and thermal conductivity vary widely within this metastable material design space, suggesting that cation disorder may be a valuable paradigm for materials design, instead of only a source of concern for optoelectronics.

2. Samples and procedures

We made d-CZTS films via co-evaporation using effusion cells loaded with elemental Cu and Sn (Alfa Aesar, 99.999% pure), and ZnS (Alfa Aesar, 99.995% pure). We supplied elemental sulfur (Alfa, 99.9995%) with a valved cracking source. During film growth, chamber pressure was typically $\sim 2 \times 10^{-4}$ torr, and the background vapor consisted primarily of elemental sulfur. For all depositions, we set the net metal flux to 3 Å/s regardless of film composition. All films were approximately 1 μm thick and were deposited on either soda lime glass or quartz glass. We deposited films without intentional substrate heating, and with heated substrates maintained at 150, 300, and 450 °C. We refer to films grown without substrate heating as being deposited at room-temperature (room-*T*), although there is some unintentional substrate heating in the chamber due to the source ovens. We further processed films grown at room-*T* by thermal annealing in an inert atmosphere at 150, 300, and 450 °C. We made a CZTS standard (c-CZTS) by depositing a precursor film at a substrate temperature of 180 °C, and then annealing at up 600 °C in an excess of Sn and S vapor. We measure the metals composition of all films by calibrated X-ray

fluorescence (XRF), and we confirmed the composition of select films by calibrated X-ray wavelength-dispersive spectroscopy (WDS).

In **Figure 1** we present the samples studied here and the CZTS crystal structure. "Low-gap" samples have composition near stoichiometric CZTS, and apparent E_g close to 1.1 eV (for d-CZTS films, E_g determined by spectrophotometry is likely suppressed by the effects of disorder). "High-gap" samples have excess ZnS, well beyond the solid solubility limit, and E_g up to 1.9 eV. The essence of this work is how thermal processing affects the atomic structure and optoelectronic properties of disordered semiconductor alloys.
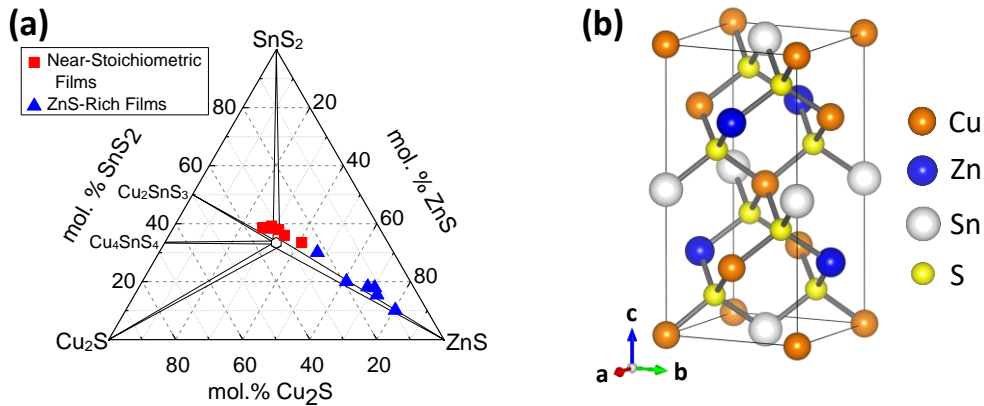
Figure 1: Non-equilibrium d-CZTS with wide composition range, samples studied here, and the CZTS crystal structure. (a) Cu_2S-SnS_2-ZnS ternary equilibrium phase diagram at 670 K, after Olekseyuk *et al*.[20] Samples studied here are low- gap, near-stoichiometric (red points) and high- gap, ZnS-rich (blue points). We study samples with varying thermal treatments at temperatures between room-T and 450 °C, as described in the text. (b) Kesterite phase of CZTS with space group $I\bar{4}$.

We measured the thermal conductivity of these CZTS films with time-domain thermoreflectance (TDTR).[21,22] TDTR is a pump-probe technique that utilizes sub-picosecond laser pulses emanating from a Ti:Sapphire oscillator at an 80 MHz repetition rate to excite and monitor temperature changes on the surface of the sample. We modulate the "pump" pulses in our TDTR measurements using an electro-optic modulator at 8.8 MHz to induce periodic, delta-function-like temperature rises on the sample surface. The "probe" pulses monitor the temporal temperature decays and oscillations from these modulated pump pulses, enabled by a mechanical delay stage that delays the arrival of the probe pulses relative to that of the pump pulses at the sample surface. We monitor the temporal changes in reflectivity of the sample due to the impulse and periodic temperature excursions induced from the pump pulses via changes in measured probe pulse intensity, using a lock-in amplifier triggered to the modulation frequency of the pump. Prior to TDTR measurements, we deposit ~80 nm of electron beam-evaporated Al on the surface of the CZTS samples to transduce the optical energy absorbed from the laser pulses into temperature changes, while forcing the majority of the optical energy to be absorbed near surface of the sample.[23] We coaxially focus the pump and probe pulses to 9 and 5 μm $1/e^2$ radii, respectively, on the surface of the sample, and limit the average powers of the pump and probe to 10.5 and 5.0 mW, respectively; this restricts the steady state temperature rise in the sample from the TDTR

measurement to < 17 K, which we calculate from the numerical solution to the cylindrical heat equation applied to our precise Al/CZTS sample geometry.[24]

We analyze the TDTR data (ratio of the in-phase to out-of-phase thermoreflectance signals *vs*. pump-probe delay time) with a cylindrically symmetric, multilayer thermal model based on the solution to the heat equation in the frequency domain.[21,25,26] We fit our thermal model to the TDTR data by iterating the assumed value of the CZTS thermal conductivity until achieving a best-fit. We also adjust the value of the thermal boundary conductance between the Al transducer and the CZTS, although, due to the relatively low thermal conductivities of the CZTS, we find that the measurements are relatively insensitive to the thermal boundary conductance. We assume literature values for the heat capacities of the Al and CZTS, and calculate values of the thermal conductivity of Al transducer from the Wiedemann-Franz law applied to four-point probe electrical resistivity measurements.[27–29] Due to the thickness of the CZTS and the relatively high modulation frequency of the pump pulses, the thermal penetration depth during our TDTR measurements is much less than the CZTS film thicknesses, and thus we are insensitive to the thermal properties of the substrate in our TDTR analyses.[25]

We performed XAS experiments on the sulfur K-edge at beamline 4-3 of the Stanford Synchrotron Radiation Laboratory (SSRL), and on the metal K-edges at beamline 20-BM of the Advanced Photon Source (APS). All XAS data was measured by fluorescence yield with samples at room temperature in a helium atmosphere. The thickness of all d-CZTS films was ~1 μm, which is well-matched to the absorption length of sulfur K-edge characteristic X-rays (approximately 0.75 μm above the K-edge) and is much smaller than the absorption lengths of the metal characteristic X-rays. For the metal K-edge measurement we focused on the EXAFS region. For the sulfur K-edge measurement we measured detailed EXAFS and XANES spectra. To assist with XANES decomposition we measured sulfur K-edge spectra for binary materials in powder form (ZnS, SnS, Cu_2S, and CuS), we obtained spectra of SnS_2 from the experimental literature, and we obtained spectra for ternary compounds Cu_2SnS_3 and Cu_3SnS_4 from theoretical calculations.[30–32]

We performed XRD experiments in Bragg-Brentano geometry using a Rigaku SmartLab system with Cu K-alpha radiation. All films measured by XRD were grown on fused quartz, and we measured a bare, fused quartz substrate from the same supplier to determine the XRD background. We prepared cross-sectional TEM lamellae via standard focused-ion beam (FIB) liftout procedures using a Zeiss NVision 40 FIB/SEM. We carried out bright-field TEM imaging on a JEOL 2100F instrument at an accelerating voltage of 200 kV.

3. Experimental results and analysis

3.1. Tunable electrical and thermal conductivity

Our d-CZTS films with greatly-expanded composition range relative to equilibrium CZTS (**Figure 1**) also feature greatly-expanded ranges of other physical properties. In **Figure 2a** we summarize our results (reported previously) that d-CZTS films can be grown with band gap in the range 1.1 – 2.8 eV, and carrier concentration in the range $1 \times 10^{16} – 3 \times 10^{21}$ cm^{-3}.[14] In **Figure 2b** we present the range of thermal conductivity (κ) measured for d-CZTS. We measured low-gap samples grown at room-*T* and then annealed at temperature up to 450 °C, high-gap samples with

growth temperature between room-T and 450 °C, and the c-CZTS standard. We find that for this set, κ varies in the range of ~0.4 – 0.8 W·m^{-1}·K^{-1}. Our measured value for c-CZTS is 0.69 ± 0.22 W·m^{-1}·K^{-1}, which is on the low-end of the range reported to-date for CZTS, as shown in **Figure 2b**. The measured thermal conductivities of each sample are tabulated in **Table S9**. The thermal conductivities of the low-gap and high-gap samples, which vary in stoichiometry, show relatively similar thermal conductivities within uncertainty. This implies that stoichiometry is not impacting the thermal conductivity for a given processing condition within the uncertainty of our measurements. However, comparing the near-stoichiometric, low-gap films, the c-CZTS has a slightly higher thermal conductivity as compared to the d-CZTS series. While the measured thermal conductivities among these low-gap samples are within uncertainties, this increase in the mean value of c-CZTS compared to those of the other d-CZTS samples could imply cation disorder impacting the phonon thermal conductivity, a finding that has previously been computationally realized via molecular dynamics calculations (including for CZTS), and indirectly concluded from studies of metallic alloys.[11,33–36]

Among the d-CZTS series of samples, we observe a general trend of a reduction in thermal conductivity with an increase in stacking fault probability, as we show in **Figure S1**. Consistent with prior studies on the phonon thermal conductivity of solid solutions mentioned above, the broad spectrum of vibrations that contribute to the thermal conductivity of multiple cation solutions means that a fraction of the vibrational spectrum with length scales longer than the length scale associated with the nearest neighbor cation disorder will contribute to the thermal conductivity.[37–40] Indeed, this is consistent with our finding of the d-CZTS samples' thermal conductivities trending with stacking fault probability, and consistent with prior works showing that crystalline coherence length-affecting defects can influence the thermal conductivity of polycrystals.[41] Thus, we conclude that the thermal conductivity of the d-CZTS samples are limited by some combination of the structural disorder from stacking faults and the chemical inhomogeneity from random cation ordering.

Our finding that κ can be substantially affected by cation disorder is consistent with previous studies on how varying the metals composition affects κ and the thermoelectric performance of CZTS.[11,42] Our thermal conductivity measurements on d-CZTS, combined with previously-published results for CZTS, show that this material system covers a very large range of κ, which may be of-interest for thermoelectric applications.[42,43]
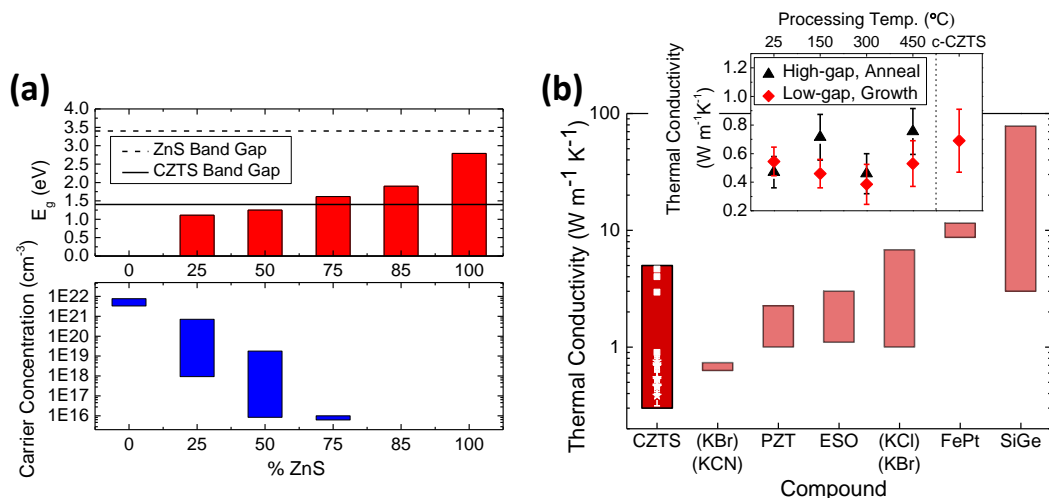
Figure 2: Tuning the optical, electrical, and thermal properties of metastable alloys with cation disorder. (a) Band gap and electrical properties for d-CZTS films with variable ZnS mole fraction, as reported previously.[14] Top panel shows band gap determined from Tauc analysis for samples grown at room-*T* with varying ZnS composition; reference values for ZnS and CZTS are indicated. Bottom panel shows estimated carrier concentration ranges for samples grown at room-*T*. For each ZnS composition, the vertical bar indicates the carrier concentration range achieved with varying Cu:Sn composition. (b) Variation in thermal conductivity for d-CZTS films and for CZTS as previously-reported, compared to ranges of thermal conductivity reported for other material systems. All data are thermal conductivity measured at room-*T*. The range for CZTS is defined by our measurements on d-CZTS (white stars, with error bars) and by previously-published measurements on CZTS (white squares). All data besides d-CZTS are from the literature; $(KBr)_{1-x}(KCN)_x$, $PbTi_xZr_{1-x}O_3$ (PZT), entropy-stabilized oxides (ESO), $(KCl)_{1-x}(KBr)_x$, ordered and disordered FePt, and Si_xGe_x.[33,37,39,40,44] The previously-published CZTS data include: sintered powder (κ = 4.7 $Wm^{-1}K^{-1}$);[42] sintered nanocrystals (κ = 2.95 $Wm^{-1}K^{-1}$);[43] thin films, fully and incompletely sulfurized (κ = 4 and 0.9 $Wm^{-1}K^{-1}$, respectively).[45] The d-CZTS samples include low-gap samples grown at room-*T* and then annealed at temperature up to 450 °C, and high-gap samples with growth temperature between room-*T* and 450 °C.

3.2. XANES: Identifying secondary phases by spectral fingerprints

In **Figure 3a** we present sulfur K-edge XANES data for our samples and standards. XANES spectra are a fingerprint of electronic structure, and change in characteristic ways with chemical trends. For instance, filling 3p orbitals of sulfur anions by ionic bonding causes a reduction in the intensity of the dipolar 1s-3p absorption feature that frequently appears as a strong pre-edge peak in the sulfur K-edge absorption spectra. This trend can be observed in our data in moving from CZTS to ZnS, as discussed below. XANES spectra are often referenced to chemical standards to quantitatively measure phase composition, and to qualitatively understand chemical bonding. Using spectral fingerprints in this way is known as XANES dactylography. For instance, in **Figure 3b** we show that the sulfur K-edge XANES spectra for a high-gap, ZnS-rich d-CZTS sample annealed at 450 °C can be well-modeled by a linear combination of CZTS and ZnS reference spectra in approximately equal proportion, as expected for a two-phase system according to the equilibrium ternary phase diagram (**Figure 1**); Cu_2SnS_3 makes a minority contribution. These three

phases selected by the regression analysis, Cu_2SnS_3, CZTS, and ZnS, define a single line across the ternary phase diagram and are structurally-coherent. The phases not selected by the regression are either not structurally-coherent with CZTS (SnS_2, Cu_2S) or do not lie along the same line in the phase diagram (Cu_4SnS_4). We perform regression analysis using the software Athena (see **Section 3.4**).
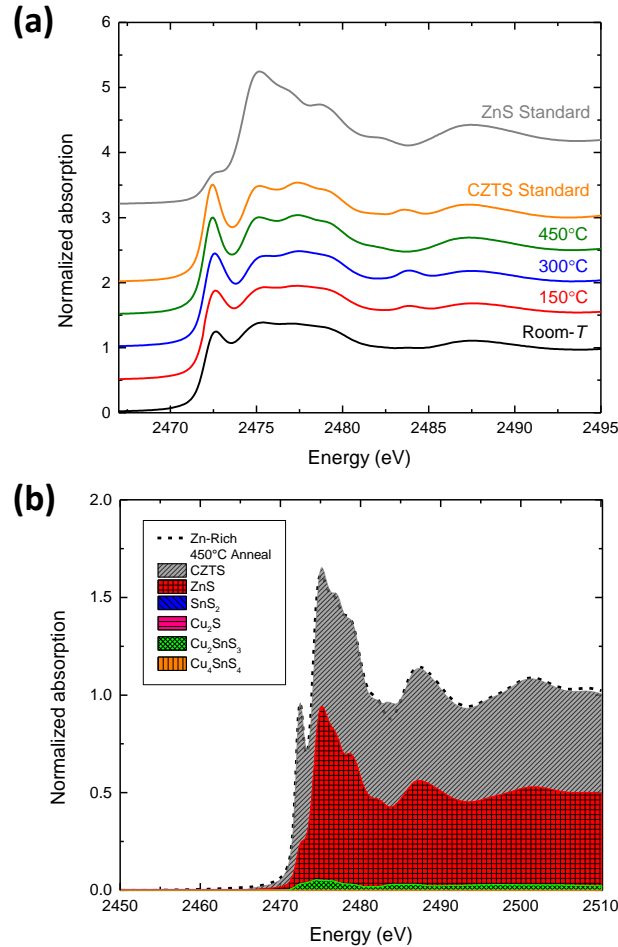
Figure 3: XANES data and dactylography. (a) Overview of XANES data collected on low-gap d-CZTS with varying post-deposition anneal temperature. Also shown are data for CZTS and ZnS standards. The XANES X-ray absorption data are processed by normalizing the edge-jump to unity, and the data sets are offset vertically for clarity. (b) Representative XANES data decomposition using a basis of crystal standards, a.k.a. dactylography. The data (black dashed line) were measured on a high-gap d-CZTS sample after annealing at 450 °C. The colored regions represent contributions of reference phases that cumulatively model the data. The sum of the contributions follows the top of the grey region and represents the best regression to the data. The individual contributions are represented by the areas of the individual colored regions: CZTS and ZnS have approximately equal representation, and Cu_2SnS_3 makes a minority contribution.

XANES dactylography is only as good as the available standards are relevant to the sample in question. For disordered samples, interpreting XANES spectra using a basis of crystal standards means that defect clusters and other disordered regions will be misidentified. For instance, the

XANES contribution of sulfur coordination tetrahedra with excess Zn, such as Cu-Zn_2-Sn or Zn_3-Sn, may be misidentified as coming from a ZnS secondary phase, due to the similarity of Zn-S bonding in CZTS and ZnS. In **Figure 4** we compare the phase composition of our samples according to XANES dactylography (columns 1 and 3) to the composition expected at equilibrium (columns 2 and 4). The equilibrium composition is determined by the equilibrium phase diagram and the overall metals composition.[20] For high-gap samples processed at high temperature, the two different analyses are in near-agreement on the phase fraction of ZnS, which is expected to be a substantial secondary phase. However, for most compositions and processing temperatures the two different analyses substantially disagree over what other secondary phases exist, and in what quantities. For instance, XANES dactylography frequently identifies the presence of Cu_4SnS_4, whereas this phase is never present according to the equilibrium phase diagram. In contrast, the equilibrium phase diagram frequently predicts the presence of SnS_2, which does not appear in XANES dactylography. This illustrates the extent to which cation disorder and non-equilibrium secondary phases are kinetically trapped in d-CZTS. For this particular illustration it is likely important that that Cu_4SnS_4 is structurally-coherent with CZTS, whereas the layered material SnS_2 is not: Cu_4SnS_4 can form endotaxially within a CZTS matrix. This suggests that interface energy, in addition to kinetic trapping, may be important in determining the phase fraction of d-CZTS films. The comparison in **Figure 4** highlights the lesson that, for a non-equilibrium and highly-disordered alloy system such as d-CZTS, the results of individual characterization techniques (*e.g.* XANES or composition) can mislead if considered in isolation.
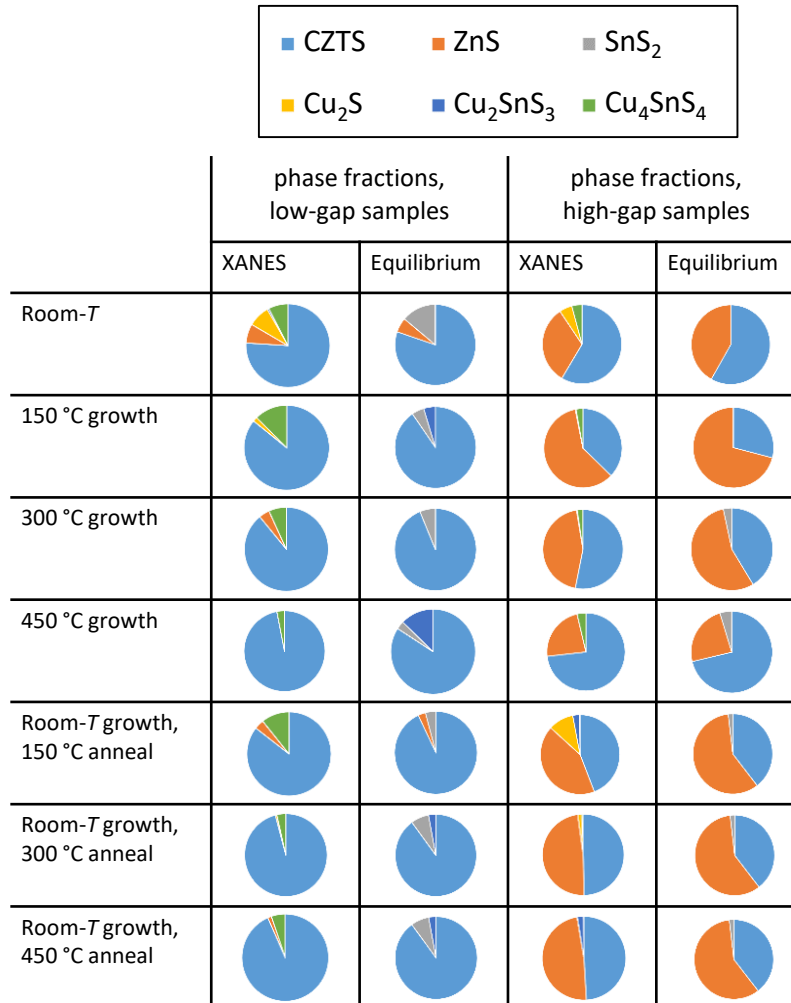
Figure 4: Phase composition determined by two methods: XANES dactylography and the equilibrium phase diagram. The XANES results are determined from the sulfur K-edge spectra by a linear combination of standards. The equilibrium results are determined from the equilibrium phase diagram.

In **Figure 5** we show a clear example of ZnS secondary phase formation with increasing growth temperature for high-gap d-CZTS. CZTS sulfur K-edge spectra have a strong pre-edge peak, indicating that sulfur 3p orbitals are partially empty. ZnS has little-to-no pre-edge peak, due to more ionic bonding and a nearly-full 3p manifold, and the XANES spectrum is dominated by the so-called near-edge peak between 1s states and the conduction band.[46] The spectra in **Figure 5** show that, as the temperature is increased, the pre-edge peak characteristic of dipolar 1S-3p absorption in CZTS is suppressed and the peak characteristic of ZnS is increased. As the processing temperature is increased, the phase composition of d-CZTS better approximates that expected from equilibrium thermodynamics, and the atomic structure of the component phases approaches that of the CZTS and ZnS standards. Therefore, while for samples processed at low temperature XANES dactylography may be misleading, it becomes more reliable for samples processed at high temperature for which the available standards are more appropriate.
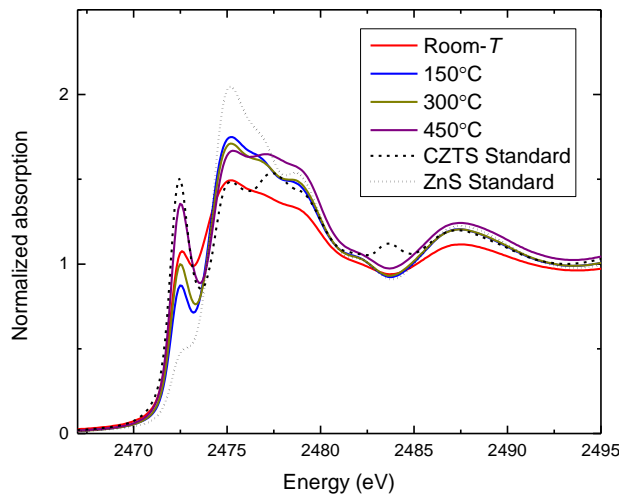

Figure 5: Emergence of ZnS secondary phase with increasing growth temperature of high-gap d-CZTS. Plotted are sulfur K-edge XANES spectra for d-CZTS films grown at substrate temperature between room-*T* and 450 °C, along with CZTS and ZnS standards. For samples processed at low temperature, XANES dactylography can be misleading, because the standards are not good models for the atomic structure and phase composition in the samples. The analysis results become more accurate as the processing temperature is increased, and the samples approach the expectations of equilibrium thermodynamics.

3.3. EXAFS: Signatures of cation disorder

EXAFS data at a given atomic absorption line are sensitive to short-range order around that element. For covalent semiconductors, pairwise bond lengths and coordination tend to be similar in crystalline and in highly-disordered (even amorphous) materials. As a result, the effect of disorder is seen most strongly in the second and higher shells of Fourier-transformed EXAFS data, corresponding to the second and higher coordination shells around the central atom.[47,48] In **Figure 6** we present K-edge EXAFS data and fits for d-CZTS samples and for the c-CZTS standard. In the spectra for all three cations (Cu, Zn, and Sn, in **Figure 6(a)**), the second shell is strongly suppressed in d-CZTS relative to c-CZTS. The second shell of the sulfur K-edge data (**Figure**

6(b)) is less strongly suppressed for d-CZTS relative to c-CZTS, as expected for a well-ordered anion lattice. The cation second-shell suppression resembles that observed for silicon amorphized by ion bombardment.[47] The cation sublattice therefore shares a description with an amorphous phase, although from this data alone one cannot conclude that d-CZTS is amorphous, and as we show below this is not the case.
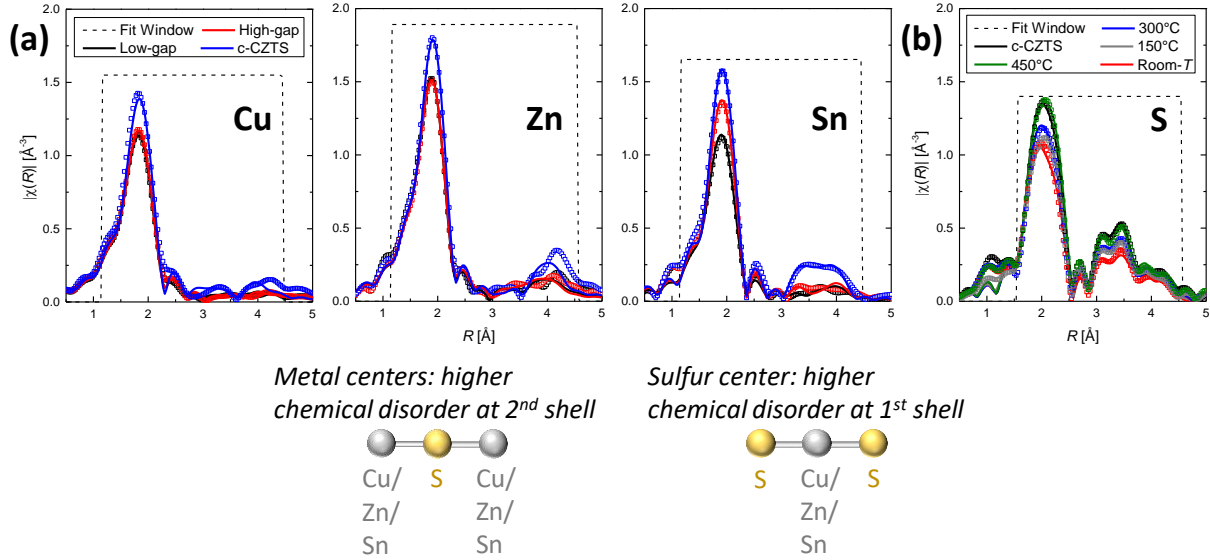
Figure 6: EXAFS data (points) and fits (lines). (a) Cu, Zn, and Sn K-edge spectra for low- and high-gap d-CZTS, as-grown at room-*T*, and a CZTS reference. (b) S K-edge spectra for low-gap d-CZTS samples with varying growth temperature. The drawings at bottom suggest how the second shell around the cations can be more disordered than the second shell around the sulfur anions due to cation disorder, as seen in the data.

3.4. EXAFS modeling

XAS data contain information on the local structure and chemical environment of the absorbing atom. We quantify short range order by fitting the extended fine-structure region of the XAS spectra to the EXAFS equation:

$$\chi(k) = S_0^2 \sum_j \frac{N_j f_j(k)}{kR_j^2} e^{-2k^2\sigma_j^2} e^{-2R_j/\lambda(k)} * \sin(2kR_j + \delta_j(k))$$

j refers to shells of like atoms, S_0^2 is the passive electron reduction factor, N_j is the number of atoms in the jth shell, k is the photoelectron wavenumber, and $\lambda(k)$ is the electron mean free path. σ_j^2 is the Debye-Waller factor (DWF), which represents the mean-square deviation of nearest-neighbor distances from the average bond length. The scattering amplitude $f_j(k)$ and the phase shift $\delta_j(k)$ are dependent on atomic number of the scattering atom. R_j is the distance to the neighboring atoms for single-path scattering, and the half-path length for multiple-scattering paths. R_j can be expressed as $R_j = R_{eff} - \Delta R_j$, where R_{eff} is the path length initially calculated from a given structural model. ΔR_j is used as one of the fitting parameters. We analyzed the XAS data

using the Demeter 0.9.24 package, containing Athena, a program for XAS data processing, and Artemis, a program for EXAFS data analysis. Background subtraction, normalization, and Fourier transformations were done by standard procedures with Athena.[49,50] We used the energy shift parameter E_0 to align the peaks of the experimentally-measured spectrum to the calculated theoretical spectrum.[51] We constructed the scattering paths from crystal structures of crystalline CZTS and ZnS and fitted them to the experimental spectra using Artemis. The EXAFS spectra for all K-Edges were fitted in the k range 3–12 and R_j range 1.15–4.55. We constrained fits using metals composition determined by XRF measurements. We fit the low-gap samples using CZTS, and the high-gap samples using a linear combination of CZTS and ZnS.

We kept the number of independent variables to a minimum, in order to obtain meaningful physical insight from EXAFS analysis. We fit low-gap samples to the third nearest-neighbor shell. Due to additional parameters from ZnS, we fit high-gap samples only to the second nearest-neighbor shell. We fixed S_0^2 at 0.68, 0.75, 0.88, and 1.0 for the Cu, S, Zn, and Sn K-edges, respectively. We obtained cation K-edge S_0^2 values from fitting EXAFS data collected on metal foils, and we took an S K-edge S_0^2 value from the literature.[52] We determined σ_j^2 and ΔR_j values for multiple-scattering paths using a combination of parameters fitted for single-scattering paths and geometric relationships. We used the assumption that Cu and Zn atoms are indistinguishable in EXAFS to add the constraint $\Delta R_{S-Cu} = \Delta R_{S-Zn}$.[19] We justify this assumption using the EXAFS fits at the Cu, Zn, and S K-edges for the low-gap samples, which showed that ΔR_{S-Cu} and ΔR_{S-Zn} were less than 0.1 Å. We further use the S K-Edge σ^2 to parametrize disorder for various coordination shells. For the high-gap samples, we justify modeling the [S]-Zn-[S] scattering paths of CZTS and ZnS as one single scattering path due to the similar Zn-S bond lengths in both compounds. We constrained N_{S-M} of respective S-M bonds using the metals composition measured by XRF, and we restricted S to be tetrahedrally-coordinated. We performed nonlinear least-squares fitting in Artemis to obtain the best-fit parameters. In **Tables S1-S8** we present the best-fit parameters for all samples and standards studied.
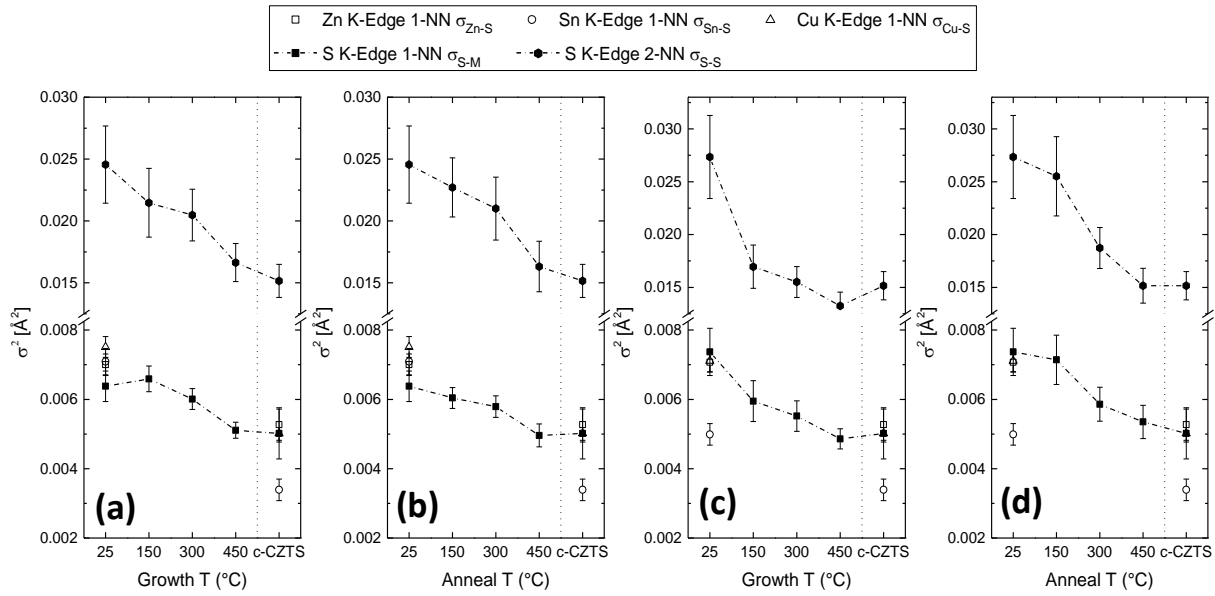
Figure 7: Debye-Waller factors (σ) determined by modeling EXAFS data for (a) low-gap, growth temperature series, (b) low-gap, anneal temperature series, (c) high-gap, growth temperature series, and (d) high-gap, anneal temperature series. σ^2 represents a mean-square deviation of bond length; it can also parameterize disorder for different coordination shells around the absorbing atom.

In **Figure 7** we show σ^2 varies with processing temperature for low-gap and high-gap samples, and for varying growth and post-growth annealing temperature. In all cases, short-range order decreases continuously for processing temperature between room-T and 450 °C, by which point it is statistically consistent with the c-CZTS reference. In all cases, disorder at the 2nd nearest-neighbor shell is stronger and decrease more quickly with temperature than the 1st nearest-neighbor shell. This is consistent with the picture derived from XRD coherence length analysis of chemical disorder on a sub-10 Å length scale in d-CZTS.

3.5. XRD data and correlation-length analysis

In **Figure 8** we present XRD data for low-gap and high-gap d-CZTS films grown at room-T and annealed at temperature up to 450 °C. With one exception, the diffraction peaks are representative of the CZTS phase; the peak near $2\theta = 27°$ is consistent with ZnS, and may also result from stacking faults (see **Section 3.6**, below). The peak intensity and width vary strongly with annealing temperature. For the samples annealed at 450 °C the peaks are narrow, and the background is flat and near-zero. For the as-grown sample without post-deposition annealing, the peaks are weak and broad, and there is substantial diffuse scattering that is strongest in the range of $2\theta = 30 - 60°$. We also observe this trend for low-gap and high-gap samples grown at varying temperature (data not shown). We identify this diffuse scattering as the result of substitutional disorder (*i.e.* a solid solution effect) on the cation sublattice, which we first analyze by its effect on diffraction coherence length.[53]

XRD is sensitive to long-range order, and complements the measure of short-range order provided by EXAFS. Diffraction peak intensity is proportional to the volume of the sample that diffracts, and the diffraction peak width measures the coherence length of the diffracting volume. Disordered samples scatter X-rays incoherently, contributing to the diffraction background and diffuse scattering, whereas crystals scatter into diffraction peaks.[53] The total scattering cross section depends only on sample composition and density. Therefore, as a material with a given composition and density becomes progressively disordered, scattering intensity is transferred from discrete diffraction peaks to the broad, diffuse pattern. Pair distribution function (PDF) analysis of total scattering provides a complete picture of short-, medium-, and long-range order, but is beyond the scope of this work.[53]
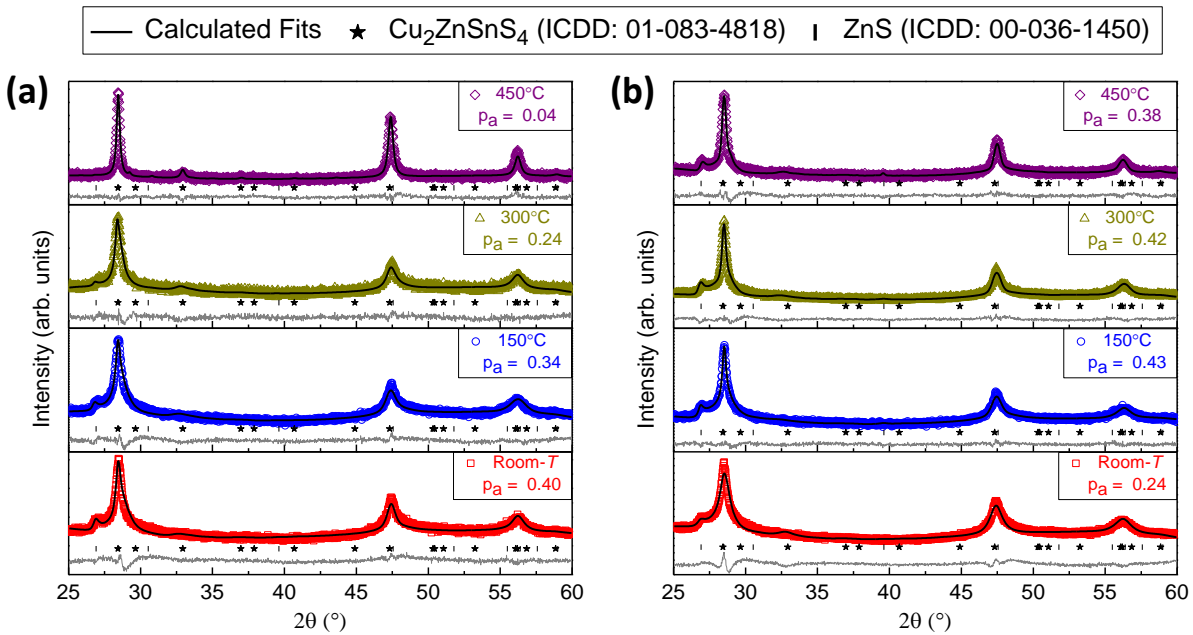
Figure 8: XRD data for (a) low-gap and (b) high-gap d-CZTS samples with varying post-growth annealing temperature. Symbols indicate peaks of reference patterns for CZTS and ZnS. The black lines show Rietveld refinement to the data using a model including probabilistic stacking faults (see **Section 3.6**); the parameter p_a is a stacking fault probability, and the grey lines are the fit residuals.

We apply a simple and general analysis of the diffraction coherence length by binning individual diffraction peaks by their linewidth. Samples processed at 450 °C have typical correlation length over 300 Å (our instrument resolution). In contrast, the room-T samples have substantial volume fraction with correlation length under 10 Å, and even the strongest discrete diffraction peaks correspond to correlation length in the range of 10 – 30 Å. Processing samples at increasing temperature (150 and 300 °C) increases the diffraction intensity and correlation length. In the Supporting Information we provide a full description of this analysis and its interpretation, including a discussion of how it compares to Williamson-Hall analysis. These results provide a view of the length scale associated with cation disorder in d-CZTS. For samples processed at low temperature, ordered regions are of $\mathcal{O}(1)$ nm, which is consistent with theoretical

simulations of entropy-driven cation disorder in this system, and with experimental observations of domains with more and less cation order.[4,11]

3.6. XRD modeling: Probabilistic Rietveld refinement, stacking faults, and endotaxy

The XRD data for most samples have a sharply-defined shoulder on the low-angle side of the (112) reflection ($2\theta = 28.441°$), which is the strongest for CZTS. This shoulder connects the CZTS (112) peak to the ZnS (100) peak ($2\theta = 26.915°$). The presence of a distinct ZnS (100) peak is expected for high-gap, ZnS-rich samples processed at high temperature, for which ZnS will form as a secondary phase according to the equilibrium phase diagram. However, the presence of this peak and the shoulder even in low-gap samples processed at low-temperature is surprising.

A sharply-defined shoulder on a particular diffraction peak (HKL) can indicate the presence of stacking faults with surface-normal direction {HKL}.[45,54,55] For CZTS, {112} is the close-packed direction (corresponding to {111} in high-temperature cubic unit cell), and the shoulder can be well-modeled as the result of a high concentration of stacking faults with {112} surface-normal. Here we show that our data are well-described by a model of CZTS with a high incidence of stacking faults along {112}.

We performed Rietveld refinement with the TOPAS-Academic v6 software using a model of hexagonal, wurtzite ZnS-like stacking faults along the {112} direction of the tetragonal, kesterite CZTS lattice. The stacking faults are modeled stochastically by a faulting probability p_a.[56] We averaged 150 randomly-generated sequences of 150-layer supercells to achieve a reasonable fit to the experimental data. We transform the tetragonal, kesterite CZTS lattice into a hexagonal pseudo-unit cell with the c-axis oriented along the kesterite {112} direction, and then use a probabilistic model of hexagonal, wurtzite ZnS-like stacking faults along this pseudo-c-axis. The transformed cell was then further reduced by taking advantage of stacking vectors away from the pseudo-c-axis direction. These transformations and reductions are for computational convenience and do not affect the outcome. We fixed the in-plane atomic positions (x and y axes) by the transformed CZTS unit cell, and allowed the pseudo-lattice parameters and out-of-plane atomic positions (z axis) to vary according to the stacking fault number. The thermal parameter, B_{eq}, was left at a constant value to minimize the number of independent variables. The absence of sharp reflections corresponding to ZnS, besides (100) that we associate with this stacking fault phenomenon along CZTS {112}, suggests that the formation of a ZnS-like fault does not preferentially seed the formation of further ZnS-like layers. In **Table 1** we show how we implement this observation in probabilistic Rietveld refinement.

| To → From ↓	CZTS	ZnS
CZTS	$1 - p_a$	p_a
ZnS	$1 - p_a$	p_a

Table 1: Constrained transition probability matrix, with increasing probability, p_a, of a fault within CZTS stacking.

In **Figure 8** we show the result of refining this model of probabilistic stacking faults to the XRD data for d-CZTS low-gap and high-gap films with varying post-deposition annealing temperature. The agreement with the data is good; we find similar agreement for samples deposited at varying temperature (not shown). This model resolves several surprising features of the XRD data and provides a microscopic picture of how d-CZTS accommodates stoichiometry variation. The model explains the sharply-defined shoulder on the low-angle side of the (112) reflection, which is not well-described by a simpler model of two, separate diffraction peaks. The model explains why only the (HKL) peak of ZnS appears in the data, even for ZnS-rich samples: d-CZTS appears to accommodate local ZnS-rich deviations from stoichiometry as stacking faults along {112} instead of endotaxial growth of a secondary phase, as suggested by previous studies on CZTS.[55,57]

The probabilistic Rietveld refinement presented here is not exclusive of other models. We chose to model ZnS-like faults, but similar agreement with the data could have been achieved with faults defined by slabs of other structurally-coherent phases including Cu_4SnS_4 and Cu_2SnS_3. This ambiguity doesn't affect our conclusion that d-CZTS accommodates local deviations from stoichiometry as stacking faults along {112}.

3.7. TEM

Cross-sectional TEM imaging of low- and high-gap samples as-deposited at room-*T* reveal the presence of many crystal grains, with length scales on the order of tens of nm. We did not locate any large (> 50 nm) areas that lacked crystalline order. Both samples contained grains with a high concentration of stacking faults, although many of the imaged grains did not contain faults; due to the nanocrystalline nature of the films, the orientation of the faults is difficult to determine. No other extended defect types were observed within the grains, nor was there any evidence of a layer of different composition or structure at either the surface or the substrate.
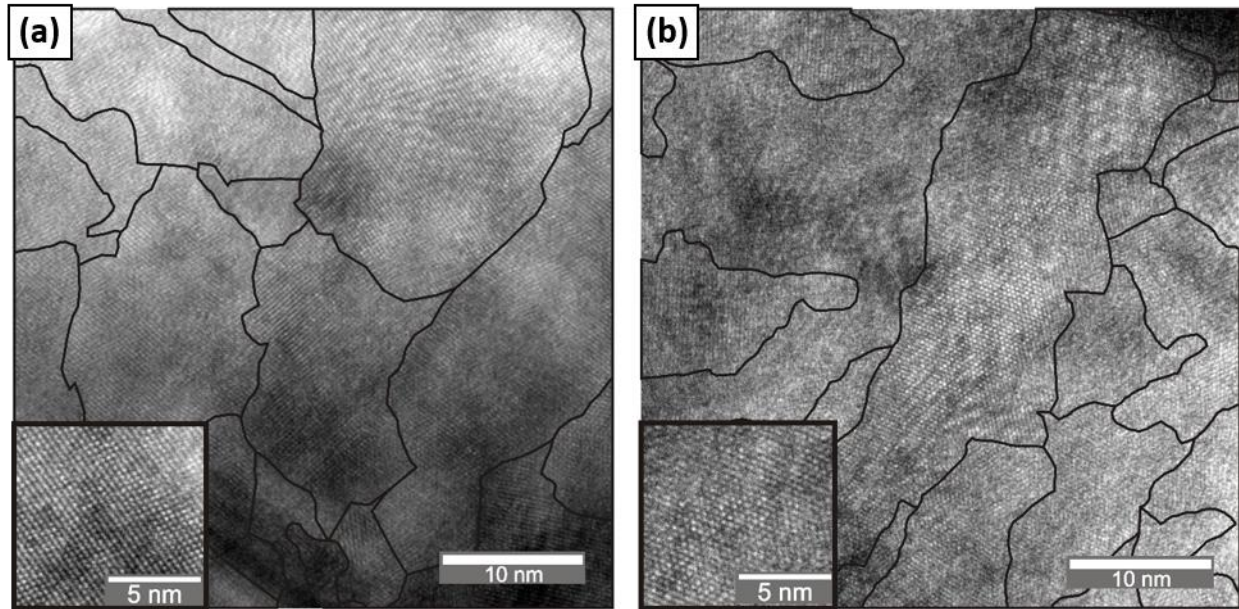
Figure 9: Cross-sectional TEM micrographs of low-gap (a) and high-gap (b) d-CZTS films, as-deposited at room-*T*. Black outlines surround each clearly-identifiable crystal grain. The insets are higher-magnification views showing coherent crystal lattices within individual grains. Both samples have lattice coherence length that is clearly much longer than 1 nm, and both samples have grains with a high concentration of stacking faults.

4. Discussion and conclusions

Chemical disorder in CZTS has been widely-studied because of its impact on PV performance, and because it presents an intellectual challenge to measurement science. Here we emphasize chemical disorder as a means to control properties by stabilizing non-equilibrium semiconductor alloys. Using low-temperature processing, we stabilize disordered CZTS (d-CZTS) films that span much of the Cu_2SnS_3 – CZTS – ZnS binary line. d-CZTS accommodates deviations from equilibrium stoichiometry by cation site disorder and a high likelihood of stacking faults along the {112} direction; even for ZnS-rich films processed at elevated temperature, the resulting material is better described as a CZTS crystal with ZnS-like stacking faults, than as a system with two distinct phases.

Our results support the conclusion that the non-equilibrium d-CZTS alloys described here are kinetically-trapped, rather than thermodynamically-metastable. CZTS at equilibrium should feature entropy-driven cation composition fluctuations on the nm-length scale, an effect which is not captured by the equilibrium ternary phase diagram.[4] However, the observed increase in cation order with increasing processing temperature suggests that d-CZTS alloys are kinetically-trapped and, with sufficient time-temperature processing, would revert towards equilibrium c-CZTS and its narrower range of physical properties. The increase in crystalline order is continuous with processing temperature, but we observe that signatures of cation disorder are little-affected by processing at 150 °C. Therefore, the expanded range of properties accessible in d-CZTS likely remains accessible for applications with operating temperatures below 150 °C. It remains to be

seen just how the physical properties (band gap, electrical and thermal conductivity, *etc*.) vary in d-CZTS at elevated temperatures.

From our research and that of many others, it is clear that the equilibrium kesterite structure is insufficient to describe real-world CZTS crystals at low temperature.[3–11,16] More complicated descriptions of cation composition fluctuations and coherent intergrowths are required to model reality, and the d-CZTS films reported here are simply an exaggerated case. In this scenario, it is unclear whether to label each d-CZTS film as a distinct phase, or to consider these samples as composites with nanometer-scale phase fluctuations. For some applications, such as those reliant only on the optical and thermal transport properties, there may be functionally no difference between these scenarios. For other applications, such as those reliant on ambipolar transport (*e.g.* solar cells), these fluctuations can be critically important.[4–6] Appropriate description may therefore depend on the intended use. In any case, CZTS remains a challenge for materials characterization.

CZTS is challenging to characterize because of the highly-disordered cation lattice and the chemical similarity between Cu^{1+} and Zn^{2+} cations. XRD signals depend more on heavy cations than on the lighter sulfur anions. Accordingly, the XRD data for d-CZTS suggests extremely small crystal coherence length, under 10 Å for samples processed at room-*T*. In contrast, TEM data shows much larger and well-ordered crystallites. The EXAFS transforms show a strongly-suppressed second coordination shell that resembles data for partially-amorphized materials. Individually, each of these techniques provides an unclear and misleading view. Our results emphasize the need for advanced characterization and to combine views from multiple techniques in order to characterize the atomic structure of cation solid solutions such as d-CZTS.

Compositional flexibility presents a means to control properties. We show that d-CZTS can be made with a very large range of band gap, electrical conductivity, and thermal conductivity. Combining our new results with the work of others', we conclude that, by virtue of its crystallographic defects, the CZTS system has exceptionally-tunable thermal conductivity. d-CZTS therefore represents a processing route to optimizing materials for opto-electronic device elements such as light absorbers, window layers, and thermal barriers.

Supporting Information

Supporting Information presents the EXAFS best-fit parameters for all samples and standards studied; measured thermal conductivity values, and dependence on stacking fault probability; XRD coherence length analysis and Williamson-Hall analysis; details of Rietveld refinement including atomic positions, transformed and reduced lattice parameters, stacking vectors, and the structures considered in stacking fault analysis; and a catalog of all samples studied and discussed in the manuscript. This material is available free-of-charge via the internet at http://pubs.acs.org.

Corresponding Author

Rafael Jaramillo, rjaramil@mit.edu

Acknowledgments

References

(1)   Wang, W.; Winkler, M. T.; Gunawan, O.; Gokmen, T.; Todorov, T. K.; Zhu, Y.; Mitzi, D. B. Device Characteristics of CZTSSe Thin-Film Solar Cells with 12.6% Efficiency. *Adv. Energy Mater.* **2014**, *4*, 1301465.

(2)   Walsh, A.; Chen, S.; Wei, S.-H.; Gong, X.-G. Kesterite Thin-Film Solar Cells: Advances in Materials Modelling of Cu2ZnSnS4. *Adv. Energy Mater.* **2012**, *2*, 400–409.

(3)   Schorr, S. The Crystal Structure of Kesterite Type Compounds: A Neutron and X-Ray Diffraction Study. *Sol. Energy Mater. Sol. Cells* **2011**, *95*, 1482–1488.

(4)   Zawadzki, P.; Zakutayev, A.; Lany, S. Entropy-Driven Clustering in Tetrahedrally Bonded Multinary Materials. *Phys. Rev. Appl.* **2015**, *3*, 034007.

(5)   Bishop, D. M.; McCandless, B.; Gershon, T.; Lloyd, M. A.; Haight, R.; Birkmire, R. Modification of Defects and Potential Fluctuations in Slow-Cooled and Quenched Cu2ZnSnSe4 Single Crystals. *J. Appl. Phys.* **2017**, *121*, 065704.

(6)   Gokmen, T.; Gunawan, O.; Todorov, T. K.; Mitzi, D. B. Band Tailing and Efficiency Limitation in Kesterite Solar Cells. *Appl. Phys. Lett.* **2013**, *103*, 103506.

(7)   Scragg, J. J. S.; Choubrac, L.; Lafond, A.; Ericson, T.; Platzer-Björkman, C. A Low-Temperature Order-Disorder Transition in Cu2ZnSnS4 Thin Films. *Appl. Phys. Lett.* **2014**, *104*, 041911.

(8)   Du, H.; Yan, F.; Young, M.; To, B.; Jiang, C.-S.; Dippo, P.; Kuciauskas, D.; Chi, Z.; Lund, E. A.; Hancock, C.; et al. Investigation of Combinatorial Coevaporated Thin Film Cu2ZnSnS4. I. Temperature Effect, Crystalline Phases, Morphology, and Photoluminescence. *J. Appl. Phys.* **2014**, *115*, 173502.

(9)   Lund, E. A.; Du, H.; Oo, W. M. H.; Teeter, G.; Scarpulla, M. A. Investigation of Combinatorial Coevaporated Thin Film Cu2ZnSnS4 (II): Beneficial Cation Arrangement in Cu-Rich Growth. *J. Appl. Phys.* **2014**, *115*, 173503.

(10)   Espinosa-Faller, F. J.; Conradson, D. R.; Riha, S. C.; Martucci, M. B.; Fredrick, S. J.; Vogel, S.; Prieto, A. L.; Conradson, S. D. Neutron Diffraction and X-Ray Absorption Fine Structure Evidence for Local Lattice Distortions and Aperiodic Antisite Substitution in Cu2ZnSnS4 Nanoparticles. *J. Phys. Chem. C* **2014**, *118*, 26292–26303.

(11)   Li, C.; Shen, Y.; Huang, R.; Kumamoto, A.; Chen, S.; Dai, C.; Yoshiya, M.; Fujii, S.; Funai, K.; Fisher, C. A. J.; et al. Hierarchically Structured Thermoelectric Materials in Quaternary System Cu–Zn–Sn–S Featuring a Mosaic-Type Nanostructure. *ACS Appl. Nano Mater.* **2018**, *1*, 2579–2588.

(12) Siah, S. C.; Jaramillo, R.; Chakraborty, R.; Erslev, P. T.; Sun, C.; Weng, T.; Toney, M. F.; Teeter, G.; Buonassisi, T. X-Ray Absorption Spectroscopy Study of Structure and Stability of Disordered (Cu SnS) (ZnS) Alloys. *IEEE J. Photovolt.* **2015**, *5*, 372–377.

(13) Just, J.; Lützenkirchen-Hecht, D.; Frahm, R.; Schorr, S.; Unold, T. Determination of Secondary Phases in Kesterite Cu2ZnSnS4 Thin Films by X-Ray Absorption near Edge Structure Analysis. *Appl. Phys. Lett.* **2011**, *99*, 262105-262105–3.

(14) Erslev, P. T.; Young, M. R.; Li, J. V.; Siah, S. C.; Chakraborty, R.; Du, H.; Lad, R. J.; Buonassisi, T.; Teeter, G. Tetrahedrally Coordinated Disordered Cu2SnS3–Cu2ZnSnS4–ZnS Alloys with Tunable Optical and Electronic Properties. *Sol. Energy Mater. Sol. Cells* **2014**, *129*, 124–131.

(15) Nozaki, H.; Fukano, T.; Ohta, S.; Seno, Y.; Katagiri, H.; Jimbo, K. Crystal Structure Determination of Solar Cell Materials: Cu2ZnSnS4 Thin Films Using X-Ray Anomalous Dispersion. *J. Alloys Compd.* **2012**, *524*, 22–25.

(16) Mendis, B. G.; Shannon, M. D.; Goodman, M. C.; Major, J. D.; Claridge, R.; Halliday, D. P.; Durose, K. Direct Observation of Cu, Zn Cation Disorder in Cu2ZnSnS4 Solar Cell Absorber Material Using Aberration Corrected Scanning Transmission Electron Microscopy. *Prog. Photovolt. Res. Appl.* **2014**, *22*, 24–34.

(17) Shi, T.; Xiao, P.; Kwon, D.-H.; Sai Gautam, G.; Chakarawet, K.; Kim, H.; Bo, S.-H.; Ceder, G. Shear-Assisted Formation of Cation-Disordered Rocksalt NaMO2 (M = Fe or Mn). *Chem. Mater.* **2018**, *30*, 8811–8821.

(18) Snyder, G. J.; Christensen, M.; Nishibori, E.; Caillat, T.; Iversen, B. B. Disordered Zinc in Zn4Sb3 with Phonon-Glass and Electron-Crystal Thermoelectric Properties. *Nat. Mater.* **2004**, *3*, 458.

(19) Zillner, E.; Paul, A.; Jutimoosik, J.; Chandarak, S.; Monnor, T.; Rujirawat, S.; Yimnirun, R.; Lin, X. Z.; Ennaoui, A.; Dittrich, T.; et al. Lattice Positions of Sn in Cu2ZnSnS4 Nanoparticles and Thin Films Studied by Synchrotron X-Ray Absorption near Edge Structure Analysis. *Appl. Phys. Lett.* **2013**, *102*, 221908.

(20) Olekseyuk, I. D.; Dudchak, I. V.; Piskach, L. V. Phase Equilibria in the Cu2S–ZnS–SnS2 System. *J. Alloys Compd.* **2004**, *368*, 135–143.

(21) Cahill, D. G. Analysis of Heat Flow in Layered Structures for Time-Domain Thermoreflectance. *Rev. Sci. Instrum.* **2004**, *75*, 5119–5122.

(22) Schmidt, A. J. PUMP-PROBE THERMOREFLECTANCE. *Annu. Rev. Heat Transf.* **2013**, *16*, 159–181.

(23) Wang, L.; Cheaito, R.; Braun, J. L.; Giri, A.; Hopkins, P. E. Thermal Conductivity Measurements of Non-Metals via Combined Time- and Frequency-Domain Thermoreflectance without a Metal Film Transducer. *Rev. Sci. Instrum.* **2016**, *87*, 094902.

(24) Braun, J. L.; Szwejkowski, C. J.; Giri, A.; Hopkins, P. E. On the Steady-State Temperature Rise During Laser Heating of Multilayer Thin Films in Optical Pump–Probe Techniques. *J. Heat Transf.* **2018**, *140*, 052801.

(25) Braun, J. L.; Hopkins, P. E. Upper Limit to the Thermal Penetration Depth during Modulated Heating of Multilayer Thin Films with Pulsed and Continuous Wave Lasers: A Numerical Study. *J. Appl. Phys.* **2017**, *121*, 175107.

(26) Hopkins, P. E.; Serrano, J. R.; Phinney, L. M.; Kearney, S. P.; Grasser, T. W.; Harris, C. T. Criteria for Cross-Plane Dominated Thermal Transport in Multilayer Thin Film Systems During Modulated Laser Heating. *J. Heat Transf.-Trans. Asme* **2010**, *132*, 081302.

(27) Touloukian, Y. S.; Buyco, E. H. *Thermophysical Properties of Matter: Specific Heat: Metallic Elements and Alloys*; IFI/Plenum: Purdue University, Thermophysical Properties Research Center, 1970.

(28) Nagaoka, A.; Yoshino, K.; Aoyagi, K.; Minemoto, T.; Nose, Y.; Taniyama, T.; Kakimoto, K.; Miyake, H. Thermo-Physical Properties of Cu2ZnSnS4 Single Crystal. *J. Cryst. Growth* **2014**, *393*, 167–170.

(29)   He, X.; Pi, J.; Dai, Y.; Li, X. Elastic and Thermo-Physical Properties of Stannite-Type Cu2ZnSnS4 and Cu2ZnSnSe4 from First-Principles Calculations. *Acta Metall. Sin.-Engl. Lett.* **2013**, *26*, 285–292.

(30)   Branci, C.; Womes, M.; Lippens, P. E.; Olivier-Fourcade, J.; Jumas, J. C. Use of X-Ray Absorption Spectra as a "Fingerprint" of the Local Environment in Complex Chalcogenides. *J. Solid State Chem.* **2000**, *150*, 363–370.

(31)   Jain, A.; Ong, S. P.; Hautier, G.; Chen, W.; Richards, W. D.; Dacek, S.; Cholia, S.; Gunter, D.; Skinner, D.; Ceder, G.; et al. Commentary: The Materials Project: A Materials Genome Approach to Accelerating Materials Innovation. *APL Mater.* **2013**, *1*, 011002.

(32)   Mathew, K.; Zheng, C.; Winston, D.; Chen, C.; Dozier, A.; Rehr, J. J.; Ong, S. P.; Persson, K. A. High-Throughput Computational X-Ray Absorption Spectroscopy. *Sci. Data* **2018**, *5*, 180151.

(33)   Giri, A.; Wee, S. H.; Jain, S.; Hellwig, O.; Hopkins, P. E. Influence of Chemical Ordering on the Thermal Conductivity and Electronic Relaxation in FePt Thin Films in Heat Assisted Magnetic Recording Applications. *Sci. Rep.* **2016**, *6*, 32077.

(34)   Giri, A.; Braun, J. L.; Tomko, J. A.; Hopkins, P. E. Reducing the Thermal Conductivity of Chemically Ordered Binary Alloys below the Alloy Limit via the Alteration of Phonon Dispersion Relations. *Appl. Phys. Lett.* **2017**, *110*, 233112.

(35)   Duda, J. C.; English, T. S.; Jordan, D. A.; Norris, P. M.; Soffa, W. A. Reducing Thermal Conductivity of Binary Alloys below the Alloy Limit via Chemical Ordering. *J. Phys.-Condens. Matter* **2011**, *23*, 205401.

(36)   Duda, J. C.; English, T. S.; Jordan, D. A.; Norris, P. M.; Soffa, W. A. Controlling Thermal Conductivity of Alloys via Atomic Ordering. *J. Heat Transf.-Trans. Asme* **2012**, *134*, 014501.

(37)   Cheaito, R.; Duda, J. C.; Beechem, T. E.; Hattar, K.; Ihlefeld, J. F.; Medlin, D. L.; Rodriguez, M. A.; Campion, M. J.; Piekos, E. S.; Hopkins, P. E. Experimental Investigation of Size Effects on the Thermal Conductivity of Silicon-Germanium Alloy Thin Films. *Phys. Rev. Lett.* **2012**, *109*, 195901.

(38)   Kim, W.; Zide, J.; Gossard, A.; Klenov, D.; Stemmer, S.; Shakouri, A.; Majumdar, A. Thermal Conductivity Reduction and Thermoelectric Figure of Merit Increase by Embedding Nanoparticles in Crystalline Semiconductors. *Phys. Rev. Lett.* **2006**, *96*, 045901.

(39)   Foley, B. M.; Paisley, E. A.; DiAntonio, C.; Chavez, T.; Blea-Kirby, M.; Brennecka, G.; Gaskins, J. T.; Ihlefeld, J. F.; Hopkins, P. E. Phonon Scattering Mechanisms Dictating the Thermal Conductivity of Lead Zirconate Titanate (PbZr1−xTixO3) Thin Films across the Compositional Phase Diagram. *J. Appl. Phys.* **2017**, *121*, 205104.

(40)   Braun, J. L.; Rost, C. M.; Lim, M.; Giri, A.; Olson, D. H.; Kotsonis, G. N.; Stan, G.; Brenner, D. W.; Maria, J.-P.; Hopkins, P. E. Charge-Induced Disorder Controls the Thermal Conductivity of Entropy-Stabilized Oxides. *Adv. Mater.* **2018**, *30*, 1805004.

(41)   Meyer, K. E.; Cheaito, R.; Paisley, E.; Shelton, C. T.; Braun, J. L.; Maria, J.-P.; Ihlefeld, J. F.; Hopkins, P. E. Crystalline Coherence Length Effects on the Thermal Conductivity of MgO Thin Films. *J. Mater. Sci.* **2016**, *51*, 10408–10417.

(42)   Liu, M.-L.; Huang, F.-Q.; Chen, L.-D.; Chen, I.-W. A Wide-Band-Gap p-Type Thermoelectric Material Based on Quaternary Chalcogenides of Cu2ZnSnQ4 (Q=S,Se). *Appl. Phys. Lett.* **2009**, *94*, 202103.

(43)   Yang, H.; Jauregui, L. A.; Zhang, G.; Chen, Y. P.; Wu, Y. Nontoxic and Abundant Copper Zinc Tin Sulfide Nanocrystals for Potential High-Temperature Thermoelectric Energy Harvesting. *Nano Lett.* **2012**, *12*, 540–545.

(44)   Beekman, M.; Cahill, D. G. Inorganic Crystals with Glass-Like and Ultralow Thermal Conductivities†. *Cryst. Res. Technol.* **2017**, *52*, 1700114.

(45)   Thompson, W. D.; Nandur, A.; White, B. E. Thermal Transport in Cu2ZnSnS4 Thin Films. *J. Appl. Phys.* **2016**, *119*, 095108.

(46)   Li, D.; Bancroft, G. M.; Kasrai, M.; Fleet, M. E.; Yang, B. X.; Feng, X. H.; Tan, K.; Peng, M. Sulfur K- and L-Edge X-Ray Absorption Spectroscopy of Sphalerite, Chalcopyrite and Stannite. *Phys. Chem. Miner.* **1994**, *20*, 489–499.

(47)   Glover, C. J.; Foran, G. J.; Ridgway, M. C. Structure of Amorphous Silicon Investigated by EXAFS. *Nucl. Instrum. Methods Phys. Res. Sect. B Beam Interact. Mater. At.* **2003**, *199*, 195–199.

(48)   Dalba, G.; Fornasini, P.; Grisenti, R.; Rocca, F. X-Ray Absorption Fine Structure: Characterization of Thermal and Structural Disorder in Non-Crystalline Solids. *J. Non-Cryst. Solids* **2004**, *345–346*, 7–15.

(49)   Ravel, B.; Newville, M. ATHENA, ARTEMIS, HEPHAESTUS: Data Analysis for X-Ray Absorption Spectroscopy Using IFEFFIT. *J. Synchrotron Radiat.* **2005**, *12*, 537–541.

(50)   Newville, M. IFEFFIT: Interactive XAFS Analysis and FEFF Fitting. *J. Synchrotron Radiat.* **2001**, *8*, 322–324.

(51)   *X-Ray Absorption: Principles, Applications, Techniques of EXAFS, SEXAFS and XANES*, 1st ed.; Koningsberger, D. C., Prins, R., Eds.; Wiley-Interscience: New York, 1988.

(52)   Gui, Z.; Green, A. R.; Kasrai, M.; Bancroft, G. M.; Stillman, M. J. Sulfur K-Edge EXAFS Studies of Cadmium-, Zinc-, Copper-, and Silver-Rabbit Liver Metallothioneins. *Inorg. Chem.* **1996**, *35*, 6520–6529.

(53)   Egami, T.; Billinge, S. *Underneath the Bragg Peaks: Structural Analysis of Complex Materials*, 2nd ed.; Pergamon Materials Series; Pergamon, 2012; Vol. 16.

(54)   Velterop, L.; Delhez, R.; Keijser, T. H. de; Mittemeijer, E. J.; Reefman, D. X-Ray Diffraction Analysis of Stacking and Twin Faults in f.c.c. Metals: A Revision and Allowance for Texture and Non-Uniform Fault Probabilities. *J. Appl. Crystallogr.* **2000**, *33*, 296–306.

(55)   Miskin, C. K.; Yang, W.-C.; Hages, C. J.; Carter, N. J.; Joglekar, C. S.; Stach, E. A.; Agrawal, R. 9.0% Efficient Cu2ZnSn(S,Se)4 Solar Cells from Selenized Nanoparticle Inks. *Prog. Photovolt. Res. Appl.* **2015**, *23*, 654–659.

(56)   Bette, S.; Takayama, T.; Kitagawa, K.; Takano, R.; Takagi, H.; Dinnebier, R. E. Solution of the Heavily Stacking Faulted Crystal Structure of the Honeycomb Iridate H3LiIr2O6. *Dalton Trans.* **2017**, *46*, 15216–15227.

(57)   Shin, S. W.; Han, J. H.; Park, C. Y.; Kim, S.-R.; Park, Y. C.; Agawane, G. L.; Moholkar, A. V.; Yun, J. H.; Jeong, C. H.; Lee, J. Y.; et al. A Facile and Low Cost Synthesis of Earth Abundant Element Cu2ZnSnS4 (CZTS) Nanocrystals: Effect of Cu Concentrations. *J. Alloys Compd.* **2012**, *541*, 192–197.